Coastal Engineering 58 (2011) 305–316

Contents lists available at ScienceDirect

Coastal Engineering

journal homepage: www.elsevier.com/locate/coastaleng

Virtual wave gauges based upon stereo imaging for measuring surface wave characteristics

Adam J. Bechle, Chin H. Wu *

Department Civil and Environmental Engineering, University of Wisconsin, Madison, WI 53706, USA

ARTICLE INFO

Article history:
Received 23 August 2010
Accepted 16 November 2010
Available online 30 December 2010

Keywords:
Virtual wave gauges
Stereo imaging
Wave height
Wave period
Wave direction
Wave reflection

ABSTRACT

A virtual wave gauge (VWG) technique based on stereo imaging is developed to remotely measure water wave height, period, and direction. VWG minimizes computational costs by directly tracking the elevation of the water surface at selected points of interest using a Eulerian based dynamic searching algorithm. Results show that the VWG technique developed in this paper dramatically improves efficiency by two orders of magnitude compared to the traditional Lagrangian–Eulerian based point cloud method of stereo image processing. VWG is tested against traditional wave wire gauges to within 98% accuracy for significant wave height. Furthermore, the flexibility of the VWG is demonstrated in two field applications. First in an offshore breaking wave case, an array of VWGs is used to efficiently measure wave directionality. Second to investigate the reflection coefficient of a rock-mounted structure interacting with nearshore waves, linear and spatial VWG arrays are designed and implemented based on *a priori* information of the wave field from a preliminary VWG measurement. Overall, we demonstrate that the flexible and computational efficient VWG technique has the potential to make real-time remote stereo imaging wave measurements a reality.

1. Introduction

Accurate measurement of wave climate is important to coastal engineering and oceanography (Holthuijsen, 2007). To well describe a sea state, information on wave height, period, and directionality is essential (Tucker and Pitt, 2001). Surface-piercing wave wire gauges and subsurface pressure transducers are commonly used to measure wave height and period. A number of these sensors are arranged as a spatial array to obtain directionality of waves. Consideration in the synchronization and spatial layout of wave arrays to avoid ambiguity in wave direction is required (Davis and Reiger, 1977). In recent years, a great deal of progress in wave measurement instrumentation has been made. For example, surface-following (Steele et al., 1992) and orbit-following buoys (Krogstad et al., 1999) are employed for long-term measurement of wave height and direction. Submerged acoustic Doppler current profilers have been developed to obtain spectral wave statistics from measured pressure, near-surface velocities, and surface displacements (Terray et al., 1999; Van Haren, 2001; Herbers and Lentz, 2010). While these advancements have led to a great success in measuring wave characteristics, maintenance and operation of *in situ* instruments in the sea remain costly and time-consuming.

Remote sensing technology is a promising tool because instrumentation does not directly contact the water or interfere with wave propagation. For example, high-frequency surface wave radars (Wyatt et al., 1999; Dankert and Rosenthal, 2004) and Light Detection and Ranging (LiDAR) systems (Hwang et al., 2000; Irish et al., 2006; Sun et al., 2005) deployed from ground, airplane, and satellite-based configurations have been used to measure wave climate. While these systems can characterize waves over a range of scales, the implementation can be prohibitively expensive. On the other hand, either active or passive optical remote sensing methods for obtaining wave climate data can be relatively cost effective.

Active optical methods, in principle, introduce a light source into the water and infer wave characteristics from the transformation of light at the water surface. Three different active optical techniques are briefly discussed here: wave profile imaging, scattered light refraction, and laser slope gauges. Wave profile imaging illuminates a wave tank with a laser light sheet to measure two-dimensional wave profiles (Yao and Wu, 2005). Scattered light refraction methods emit an underwater light and relate the intensity of the refracted light to one-dimensional wave slope (Keller and Gotwols, 1983; Jähne and Riemer, 1990; Jähne et al., 2005). Zhang and Cox (1994) captured two-dimensional wave slope by using a colored light source. To date, wave profile imaging and scattered light refraction methods have mainly been utilized in the laboratory. For the field, laser slope gauges utilizing a submerged scanning laser to provide the light source for refraction-based wave slope measurement have been developed (Palm et al., 1977; Shemdin and Hwang, 1988; Savelsberg et al., 2006). Laser slope gauges are employed to measure short capillary waves over a small coverage area on the order of 0.1 m by 0.1 m (Hara et al., 1994; Bock and Hara, 1995; Hwang et al., 1996; Frew et al., 2004).

* Corresponding author. Department of Civil and Environmental Engineering, 1269D Engineering Hall, University of Wisconsin, Madison, WI, USA. Tel.: +1 02 608 263 3078; fax: +1 608 262 5199.
E-mail address: chinwu@engr.wisc.edu (C.H. Wu).

0378-3839/$ – see front matter
doi:10.1016/j.coastaleng.2010.11.003

Nevertheless, large-scale wave climate measurement in the field with active optical methods still remains a challenging research topic (Jähne et al., 1994).

Passive optical methods utilize natural sun lighting without additional light sources and are therefore more applicable for field implementation than active methods. There are four main mechanisms observed by passive optical methods: reflection, sunglint, polarimetry, and photogrammetry. The reflection method exploits the relationship between the intensity of sunlight reflection and water surface slope to estimate spectral and directional information of wave fields (Stilwell, 1969; Gotwols and Irani, 1980). The reflection method operates best under monotonic illumination and is most suited for measuring smaller wave slopes. Sunglint methods generate probability density functions of surface slope and are less sensitive to lighting conditions (Cox and Munk, 1954; Su et al., 2002; Bréon and Henroit, 2006). Cureton et al. (2007) extended the sunglint mechanism method to compute wave power density spectra. Recently, a polarimetric imaging method (Zappa et al., 2008) was developed to estimate two-dimensional wave slope by detecting changes in the polarization of light as it reflects off of the water surface. Thus far, the polarimetric method has been performed mainly on smooth water surfaces under overcast skies.

Photogrammetry methods are based upon the geometric relationship between photographic images and topographic features of the water surface to determine wave characteristics (Holland et al., 1997; Hwung et al., 2009). For example, the well-known Argus video project quantifies nearshore wave characteristics and coastal morphodynamics (Holman and Stanley, 2007). For offshore wave climate, Kim et al. (2008) measured low frequency wave height and period in the field by tracing the motion of a distant moored buoy through a time series of video images from a single camera. Stereo imaging uses at least two images taken from different vantage points to essentially triangulate the three-dimensional coordinates of the water surface (Holthuijsen, 1983). Shemdin et al. (1988) and Banner et al. (1989) used stereo photographs to examine long wave modulation of high frequency waves. At the time, the results were restricted to wave number spectra at few instants in time because of the extensive effort required to process the images.

In recent years, improvements in computing power and camera hardware technology have promoted great progress in stereo image processing. For example, an automated trinocular stereo imaging system (ATSIS), developed by Wanek and Wu (2006), was successfully used to measure the temporal evolution of three-dimensional small-scale capillary waves and large-scale wave breaking. The trinocular arrangement of cameras and subpixel stereo matching routine implemented by ATSIS also enhance the reliability and accuracy of three-dimensional water wave measurements. Benetazzo (2006) analyzed a time-series of stereo video and provided an estimate for the systematic error caused by the quantization of the digital images. To extract a time series of the water surface fluctuation at a specified location, both Wanek and Wu (2006) and Benetazzo (2006) first processed large portions of the image to generate dense, unstructured point clouds of water surface coordinates and then interpolated elevations at specified points of interest. With a processing time of approximately 0.2 s per pixel, tremendous computational time is required to analyze a large portion of a full image (10^2–10^3 pixels), hindering the practical application of stereo imaging for real-time wave climate characterization (de Vries et al., 2009).

In this paper, an innovative virtual wave gauge (VWG) technique is proposed to improve the computational costs of stereo imaging wave measurements (Wanek and Wu, 2006). Specifically, a robust dynamic searching algorithm is developed for VWG to directly measure the water surface fluctuations at any selected point of interest in the images, mimicking the action of a physical wave gauge. Wave directionality can be easily determined with an array of VWGs prescribed based on *a priori* wave field information. Results show that the VWG technique can accurately measure wave climate statistics including wave height, period, and direction. In terms of efficiency, the computational cost of VWG is two orders of magnitude less than that of a similar measurement made with the point cloud processing technique. In the following, Section 2 details the VWG technique, including concepts of stereo imaging and the essence of the VWG algorithm. The efficiency and accuracy of the VWG is addressed with a validation experiment in Section 3. Section 4 presents the results of a wave climate measurement in offshore and nearshore environments made with VWGs. Finally, conclusions and suggestions for advancing the VWG technique are given in Section 5.

2. Stereo imaging

2.1. Automated trinocular stereo imaging system

Temporal and spatial characteristics of three-dimensional surface waves were measured using the Automated Trinocular Stereo Imaging System (ATSIS) developed by Wanek and Wu (2006). ATSIS utilizes three progressive scan IEEE-1394 CMOS cameras with a resolution of 640 × 480 pixels to capture high-quality video images of the water surface at a rate between 1 and 100 Hz. Each camera is equipped with a 16 mm C-mount lens with a horizontal view angle of 22°. The cameras sit on adjustable pan-tilt tripod heads which are attached to an inverted aluminum T-bar, allowing the cameras to be rotated to view the field of interest. An external trigger device synchronizes the three cameras. Images are recorded directly onto the hard drive of a laptop computer, making the system portable to accommodate the varying conditions of field sites. For further details on the hardware and software of ATSIS, readers can refer to Wanek and Wu (2006). In the following, we briefly overview the stereo imaging principle and point-cloud technique used in ATSIS.

A pinhole camera model is employed to quantitatively describe the relationship between an object and its associated point in the image. Fig. 1 shows the two coordinate systems: the world space, defined by the *XYZ* axis where the *XY* plane is parallel to the mean water surface with the *Z* axis perpendicularly upward, and the image space, defined on the camera's image sensor along the *UV* axis with an origin (u_0,v_0). For Camera A, a light ray passes from the object *O* at (X_o, Y_o, Z_o) to the camera's optical center at (X_A,Y_A,Z_A), mapping onto the image sensor at (u_A,v_A). The relationship among these three points on the same line is described by the collinearity equation

$$\begin{aligned} u_A-u_O &= -f_A\left[\frac{m_{11}^A(X_O-X_A)+m_{12}^A(Y_O-Y_A)+m_{13}^A(Z_O-Z_A)}{m_{31}^A(X_O-X_A)+m_{32}^A(Y_O-Y_A)+m_{33}^A(Z_O-Z_A)}\right] \\ v_A-v_O &= -f_A\left[\frac{m_{21}^A(X_O-X_A)+m_{22}^A(Y_O-Y_A)+m_{23}^A(Z_O-Z_A)}{m_{31}^A(X_O-X_A)+m_{32}^A(Y_O-Y_A)+m_{33}^A(Z_O-Z_A)}\right] \end{aligned} \tag{1}$$

where f_A is the focal length of the lens and m_{ij}^A are the rotational transformation coefficients between world and image space, composed of trigonometric functions of the rotation angles α, azimuth; τ, tilt;, and θ, swing. Readers can refer to Wolf and DeWitt (2000) for the details of these coefficients. Based upon Eq. (1), the location of an object on an image is determined from the object's location in the world space and the camera orientation parameters. Conversely, the two image coordinates (u_A,v_A) and camera orientation parameters are insufficient to determine the object's three unknown world coordinates X_A, Y_A, and Z_A. Adding one camera provides two more equations to constrain the geometry, a practice known as stereo imaging (Holland et al., 1997). In this paper, three cameras are used to yield three stereo-pairs of images. Trinocular stereo imaging effectively addresses issues of consistency and accuracy present in the binocular stereo (Dhond and Aggarwal, 1990; Bhat and Nayar, 1998). Each camera provides two equations for the same three unknowns,

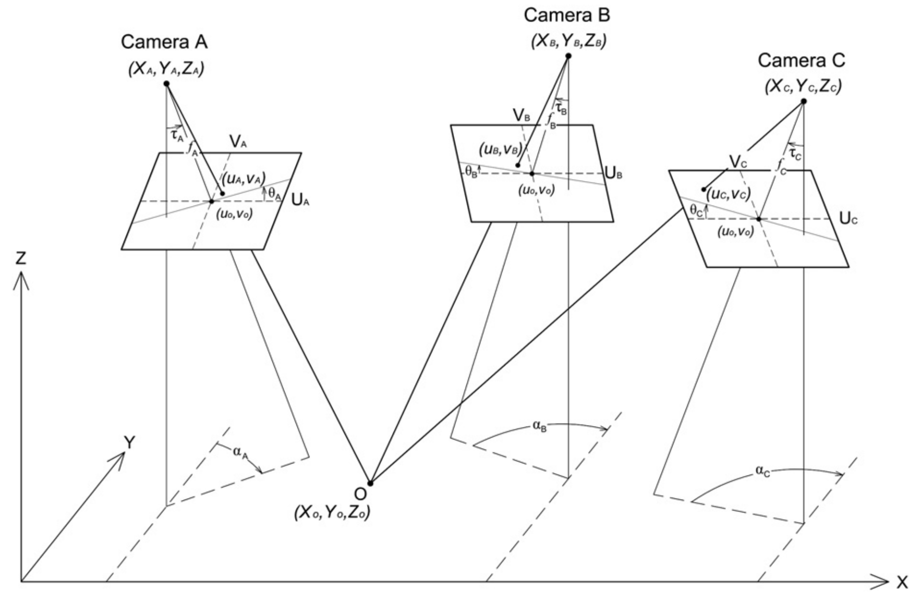

Fig. 1. Pinhole camera model for stereo imaging illustrating the collinearity relationship between the object (X_O,Y_O,Z_O), the image points (u_A,v_A), (u_B,v_B), and (u_C,v_C) and the camera's optical center (X_A,Y_A,Z_A), (X_B,Y_B,Z_B), and (X_C,Y_C,Z_C) for Cameras A, B, and C, respectively. Also shown are lens focal length, f, and camera rotation angles azimuth, α; tilt, τ; and swing, θ.

yielding a set of six equations to determine the location of water surface motions based upon a least-squares technique.

A two-step calibration procedure is performed for each camera to determine the coefficients that describe the transformation between world and image coordinates in Eq. (1). Interior calibration solves for the radial lens distortion coefficients and rectifies the images (Holland et al., 1997). Exterior calibration determines the camera orientation parameters including focal length, optical center, and rotation angles via an iterative optimization process. Because of the difficulties in obtaining accurate control points on a fluctuating water surface in the field, an in-house exterior calibration technique was proposed and successfully implemented (Wanek and Wu, 2006). First, wave images are collected in the field with camera orientations fixed with respect to each other and the aluminum T-bar leveled to ensure the XY plane is parallel to the water surface. Afterwards, ATSIS is brought back to the laboratory where the in-house calibration is performed using a precise three-dimensional control point grid (see Fig. 3 in Wanek and Wu, 2006). The only relative difference between in-house and field camera orientations is azimuth rotation angle which can be determined with a compass.

Stereo matching is performed to determine the three-dimensional coordinates of a specified point on the water surface. First, a square candidate window is centered on the point of interest in image A. The corresponding point in Image B is found by moving an identically sized search window through Image B to locate the point with the highest normalized cross correlation (NCC) coefficient (Scharstein and Szeliski, 2002; Brown et al., 2003). To improve efficiency, the search window is moved along the epipolar line between Image A and Image B, constraining the possible corresponding point to a one-dimensional problem (Forsynth and Ponce, 2003). Furthermore, to refine the pixel-level NCC match, a sub-pixel matching routine is implemented by fitting a non-linear, affine relationship between the intensity values of the candidate and search windows, yielding the optimal fractional pixel location of the corresponding point (Wolf and Dewitt, 2000). While the sub-pixel refinement requires approximately one order of magnitude more processing time in comparison with the normal NCC match, the accuracy of the water surface coordinates can dramatically improve (Wanek and Wu, 2006). For trinocular stereo imaging, matching is performed using three image pairs (i.e., AB, BC, and AC) to determine the corresponding image points.

To obtain fluctuations of water surface elevation, Z_m, at a measurement point of interest (MPOI) located at (X_m,Y_m), past studies (Benetazzo, 2006; Wanek and Wu, 2006) use a point cloud technique. The point cloud technique is based upon a Lagrangian–Eulerian stereo imaging approach, where the Lagrangian component uses stereo matching to obtain an unstructured point cloud of water surface coordinates from which the Eulerian component interpolates the water surface elevation at the MPOI. As the water surface at the MPOI oscillates vertically with the waves, the position of the MPOI in the image thereby moves. As a result, the area of point cloud needs to be large enough to include to all possible positions of the MPOI in the image. Generally the point cloud size requires approximate 300 matching points. In this paper, an efficient technique is developed to reduce the high computation cost associated with the large amount of required matching points.

2.2. Virtual wave gauge (VWG)

The development of the virtual wave gauge (VWG) technique is aimed at improving the efficiency of tracking water surface fluctuations at an MPOI. Unlike the point cloud method, the VWG technique is based upon a Eulerian approach to measure the elevation of the water surface Z_m at the MPOI. Fig. 2 illustrates the VWG, defined as a vertical line at the MPOI, representing all possible elevations of Z_m in the world space. In other words, the VWG essentially functions as a physical wire wave gauge placed vertically in the water. The VWG is bounded by the maximum and the minimum water surface elevation estimates, i.e.,

$$Z_{max} = \overline{Z}_E + \Delta Z, \tag{2a}$$

$$Z_{min} = \overline{Z}_E - \Delta Z, \tag{2b}$$

where $\overline{Z}_E$ is an estimate of the mean water surface elevation and ΔZ is the maximum expected wave amplitude. The VWG in the world space is projected onto images A and B with Eq. (1), representing all possible image coordinates of the water surface at the MPOI (see the upper left and right in Fig. 2, respectively). If the location of the water surface at the MPOI can be identified, e.g. with a surface float, Eq. (1) would be constrained and Z_m could be found. In most cases, there is no physical

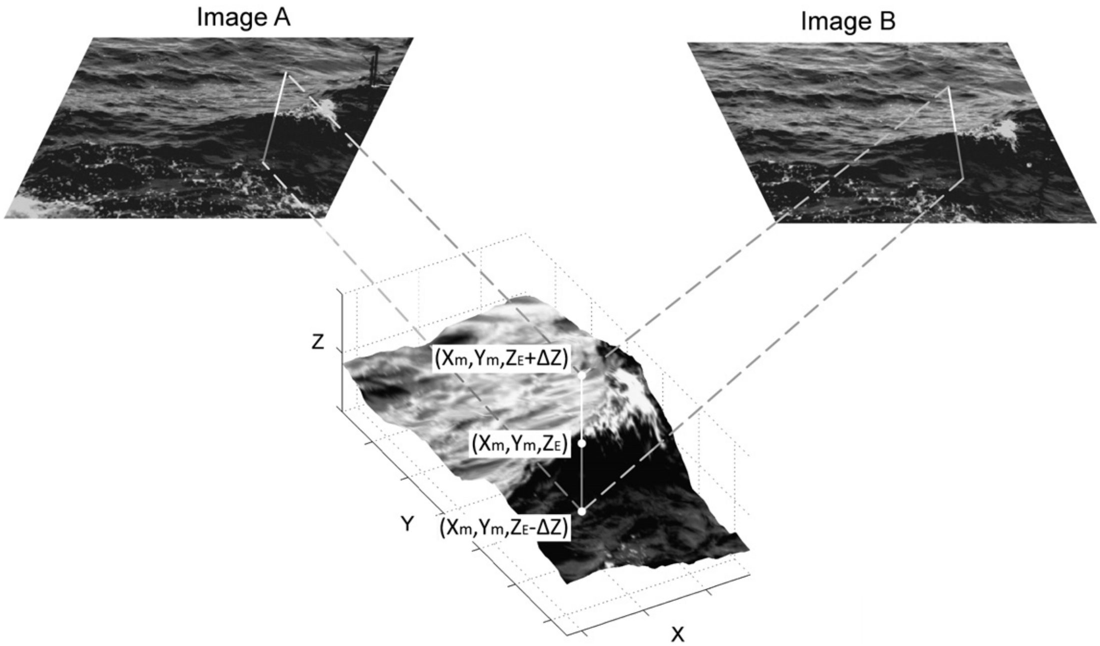

Fig. 2. Virtual wave gauge concept, in which the water surface at the measurement point of interest (X_m,Y_m) must exist on a vertical line between the maximum and minimum water surface estimates Z_{max} and Z_{min}. The virtual wave gauge image line projects onto the images as a straight line.

indicator to track the water surface position along the VWG, yielding a moving free-surface problem. In the two camera instances, this gives 4 equations with 5 unknowns: u_A, v_A, u_B, v_B, and Z_m. Stereo matching at the moving free-surface is needed to provide additional constraints to determine Z_m. For efficiency, a dynamic searching algorithm is developed to locate the water surface at the MPOI. The concept is to iteratively approach the free-surface location using a weighted bisection method to choose points on the VWG to stereo match until the MPOI is found.

Fig. 3 illustrates the dynamic searching algorithm, shown for binocular stereo for brevity. First, we project points 1, 2, and 3 onto Image A: the maximum point Z_{max}, the minimum point Z_{min}, and an estimate for the water surface elevation Z_E, taken initially as the mean water surface (see Fig. 3a). The corresponding world coordinates of these three image points are determined from stereo matching. If the horizontal world coordinates (X_i,Y_i) of any of the three initial points coincide with the MPOI (X_m,Y_m), the water surface elevation Z_m is thereby determined. More likely, the world coordinates of the three initial points are located elsewhere on the XY plane, as seen in Fig. 3b. In this case, the MPOI lies between points 2 and 3, which form a bracketing pair. A new estimates for the image coordinates of the MPOI (u_4,v_4) in Fig. 3c are updated using a weighted bisection between the image coordinates of the bracketing pair (u_2,v_2) and (u_3,v_3):

$$u_m = \left(\frac{d_3}{d_2 + d_3}\right)u_2 + \left(\frac{d_2}{d_2 + d_3}\right)u_3, \tag{3a}$$

$$v_m = \left(\frac{d_3}{d_2 + d_3}\right)v_2 + \left(\frac{d_2}{d_2 + d_3}\right)v_3, \tag{3b}$$

where d_2 and d_3 are the horizontal world coordinate distances between the MPOI and bracketing points 2 and 3, respectively. The actual world coordinates of point 4 are determined by stereo matching (Fig. 3d) and are used to form the next bracketing pair around the MPOI; in this case, points 3 and 4 form the updated bracketing pair. Using Eqs. (4) and (5) with this new bracketing pair of points 3 and 4, we refine the estimated image coordinates of the MPOI, denoted as point 5 (Fig. 3e). Similarly, the corresponding world coordinates of point 5 is determined by stereo matching (see Fig. 3f). This process is repeated until the world coordinates of the ith point (X_i,Y_i) converge to those of the MPOI, (X_m,Y_m) under a tolerance criterion ε. In this study ε = 1.0 cm is chosen due to the pixel resolution. At last, the water surface elevation at the MPOI, Z_m, is taken to be Z_i.

To further save computation for the subsequent time steps, we reuse the world coordinates of the original maximum and minimum points 1 and 2. The current water level measurement Z_m is used as a new estimate for the water surface elevation Z_E at point 3. Based upon this procedure, it is found that an average of 3–5 iterations is typically required to reach the convergence criterion. In comparison to the hundreds of points used in the point cloud area technique, the dynamic searching algorithm of the Eulerian-based VWG reduces the computational time by approximately two orders of magnitude. The VWG technique greatly improves the efficiency, making real-time surface water wave measurement feasible.

3. Validation

A capacitance type wire wave gauge (Richard Brancker Research Ltd.) with the digitalized resolution of 0.51 mm was used to sample water surface displacements at the rate of 16 Hz in Lake Mendota in Madison, WI. Meanwhile, ATSIS was deployed on an observation deck 2.2 m above the water surface to collect images for this study. The cameras acquired images at 15 frames per second with a baseline between cameras of 43 cm. The wind condition was recorded to be 3.1 m/s from the west–northwest. The MPOI for the VWG was (X_m,Y_m) = (0.55 m, 3.25 m), which was the location of the wire wave gauge as determined by stereo matching. The VWG technique was applied over the duration of 45 s, a total of 675 images.

Fig. 4a shows the time series of surface displacements measured by the VWG and wire wave gauge. The mean absolute measurement difference between VWG and the wire wave gauge is 1.1 cm. This difference is less than the image quantization error of 1.8 cm, which is based on camera orientation and resolution (Benetazzo, 2006). Using an average up-crossing/down-crossing method, the significant wave height of the time series was 15.8 cm for the VWG and 16.1 cm for the wire gauge, a 1.9% relative difference. The mean absolute difference relative to significant wave height is similar to

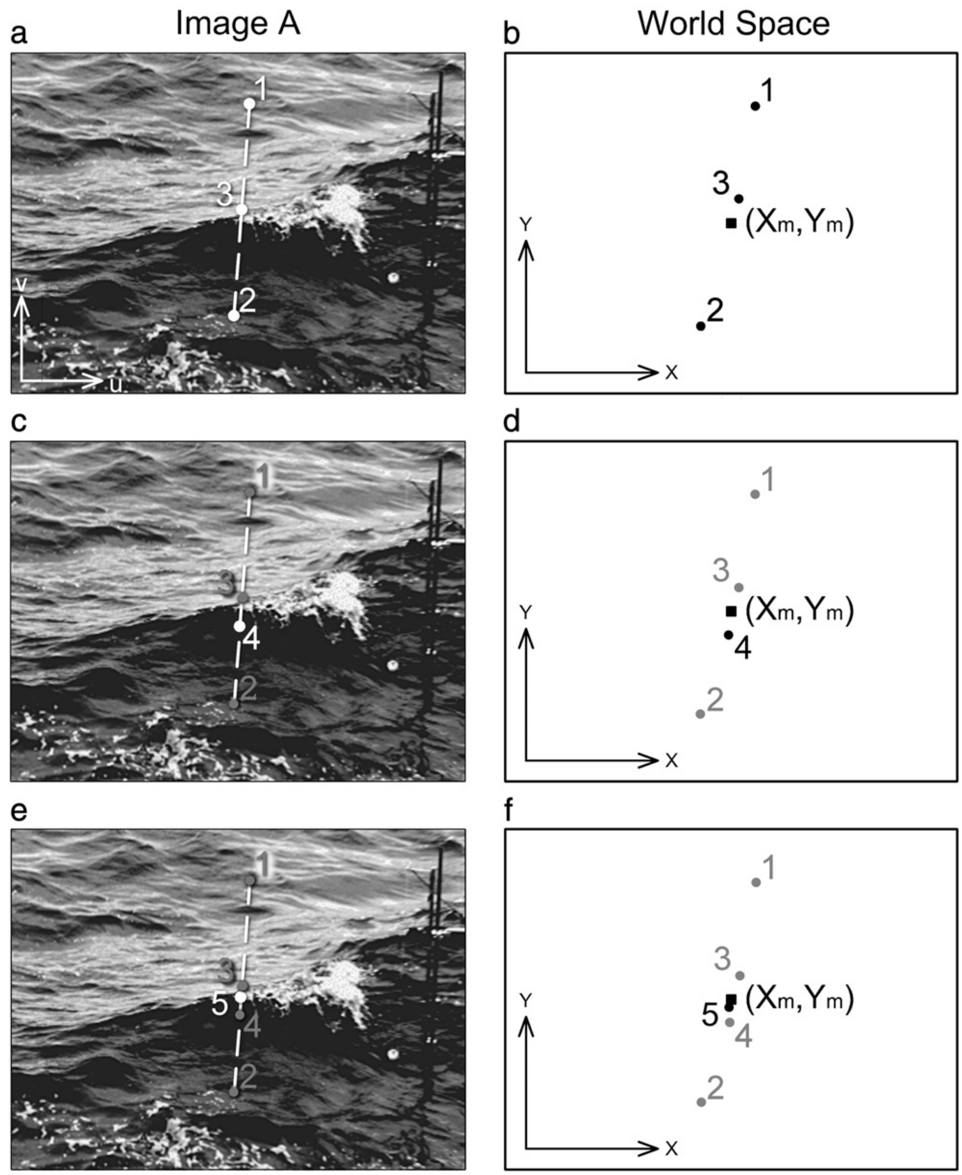

Fig. 3. Virtual Wave Gauge procedure, in which (a) points 1, 2 and 3 are defined in Image A and (b) stereo matched to provide the world coordinates. A weighted bisection method is applied to the world coordinates of the bracketing points 2 and 3 to estimate (c) the location of (X_m,Y_m) in the image as point 4 and (d) stereo matched to give a new world coordinate. Weighted bisection applied to bracketing points 2 and 4 gives (e) image point 5, which is then (f) stereo matched. This process is repeated until convergence is achieved between a matched point in world space and the measurement point of interest (X_m,Y_m).

the relative difference between a binocular stereo imaging measurement and an ultrasonic wave gauge (Benetazzo, 2006). Overall, the difference between the VWG and the wire wave gauge is almost indistinguishable, indicating the success of the VWG algorithm to accurately measure water waves.

Fig. 4b shows the time series of water surface displacement obtained by the point cloud method and the VWG technique. The measurements obtained by both methods are almost identical. The mean absolute difference in water surface elevation is 0.7 cm. The significant wave height computed with the point cloud method is 15.4 cm, a 2.5% difference from VWG measurement. In terms of computational cost, the point cloud method required 258 stereo matched points per time step to cover the all possible positions of the MPOI in the images whereas the VWG technique only uses an average of 3.8 stereo matched points per time step to obtain water surface elevation at the MPOI. As a result, the Eulerian-based VWG technique is more efficient than the Lagrangian–Eulerian-based point cloud method by approximately two orders of magnitude. With accuracy comparable to that of a physical wave-wire measurement, the VWG technique is proven to be operationally feasible for real-time wave measurements in the field.

4. Applications

The VWG technique is applied in two field experiments on Lake Mendota, Wisconsin to demonstrate the flexibility and efficiency of the method. First, we employ the VWG technique in an array arrangement to measure the direction of wave propagation under an offshore breaking wave climate. Second, we use the VWG array to examine nearshore waves interacting with a stone-mounted structure. The reflection coefficient of the structure is calculated using both linear and spatial arrays of VWGs.

4.1. Offshore breaking waves

ATSIS was used to capture images of an offshore breaking wave condition under 5.7 m/s northwest winds. The cameras, situated 5.2 m above the water surface with a 61 cm baseline, acquired images at

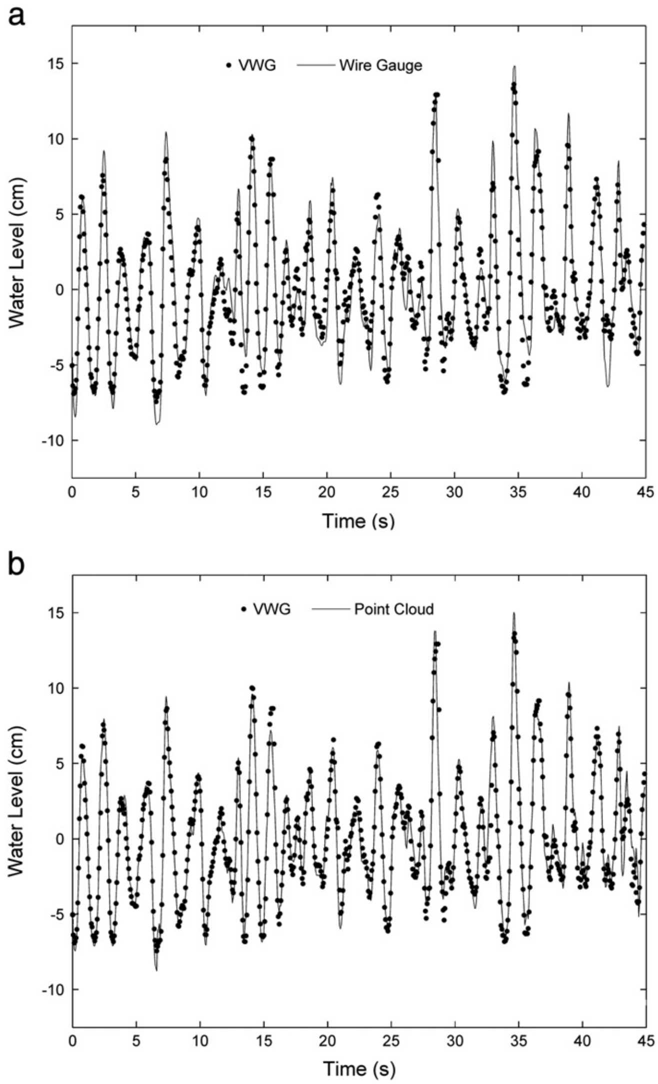

Fig. 4. Time series comparison between (a) the VWG and the wire wave gauge and (b) the VWG and point cloud.

10 Hz. To measure wave directionality in addition to height and period, an array of VWGs is formed. Preliminary analysis of wave climate with stereo imaging estimated the wavelength of the dominant waves to be 4.1 m. Based upon this *a priori* information, a right triangle array of VWGs A, B, and C is formed with an orthogonal spacing of 0.5 m (see Fig. 5), following the guideline suggested by Tucker and Pitt (2001). To observe the shoreward propagation of the waves, a VWG D is added far from the triangular array. In the following, the wave climate is characterized using both time-series and spectral analyses.

First, Fig. 6 shows the time series of the water surface displacement at locations A, B, C, and D, obtained from performing the dynamic searching algorithm on a time series of 300 recorded images. It is apparent that the VWG D, located furthest offshore, encountered the waves well before the other gauges. Subsequently, the waves reached VWG B next and then VWG C, suggesting that the waves propagated primarily along the direction of VWGs B and C toward the shore. The time difference of surface displacements between VWG A and VWG C is at times almost indistinguishable, indicating there was a significant lateral wave component along the direction of VWGs A and C, the cross-shore direction. To quantify the direction of wave propagation, we calculate the individual wave arrival time within the triangular array. The time series is processed using a bandpass filter centered on the peak wave period with a bandwidth of 0.2 Hz. The time stamps associated with both crests and troughs of the filtered waves are thereby identified. The time difference between wave crest (or trough) arrival at the central VWG B and the peripheral VWGs A and C is found as Δt_{BA} and Δt_{CB}, respectively. These time lags, in conjunction with the distance between the gauges L_{BA} and L_{CB}, are used to calculate the direction of wave propagation

$$\theta = \tan^{-1}\left(\frac{L_{CB}/\Delta t_{CB}}{L_{BA}/\Delta t_{BA}}\right). \quad (4)$$

Averaging the values based upon wave crests and wave troughs gives the wave propagation direction of $-60° \pm 1°$ in reference to the horizontal, consistent with the wind direction. The results demonstrate that an array of VWGs using time series analysis can effectively measure the wave propagation direction.

Second, the directional spectrum of the wave field is obtained using spectral analysis. The directional spectral density function is defined as the wave energy distributed across both frequency and spatial domains

$$S(f,\theta) = S(f)\cdot G(f,\theta), \quad (5)$$

where $S(f)$ is the frequency spectrum and $G(f,\theta)$ is the directional spreading function. Several methods including Extended Maximum Likelihood Method (EMLM), Extended Maximum Entropy Principle (EMEP), and Bayesian Directional Method (BDM), have been developed

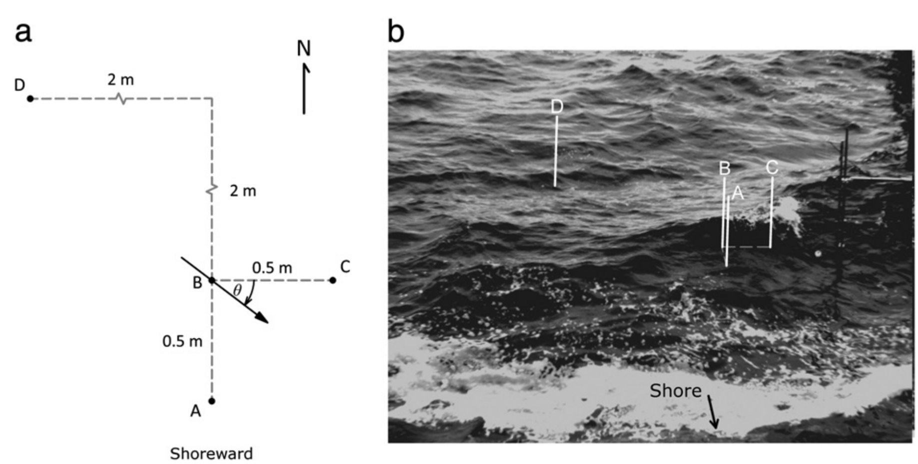

Fig. 5. (a) VWG array setup, where a right triangle array is formed with VWGs A, B, and C while VWG D is located in the distance to further observe the wave propagation through space. (b) The VWG array is projected onto the image.

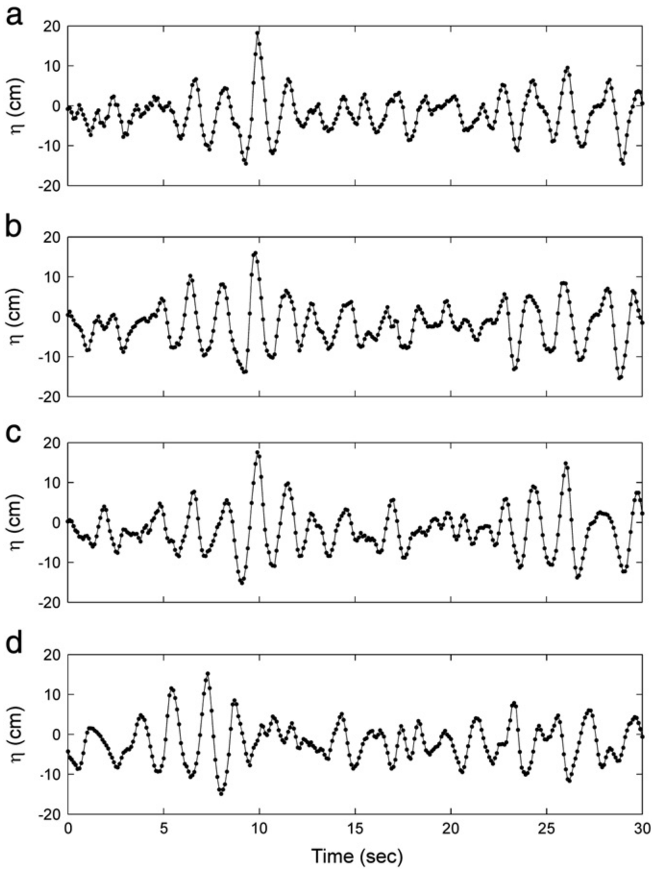

Fig. 6. VWG array time series corresponding to gauge locations in Fig. 5.

to estimate directional spectrum. Comparisons among methods suggest that EMEP and BDM provide more focused and less noisy estimates of the directional spectrum than EMLM (Benoit and Teisson, 1994; Hashimoto, 1997; Huang et al., 2003). In this paper, we choose EMEP over BDM to compute the directional spectrum to achieve a balance of directional resolution and computational efficiency.

To determine the directional spectral density function, we implement the EMEP technique using the DIrectional WAve SPectra Toolbox DIWASP (Johnson, 2008). The time series of VWGs A, B, and C are processed using a frequency bandwidth of 0.05 Hz and a directional resolution of 1°. Fig. 7 shows the contour plot of the direction spectrum. The peak of the directional spectrum is located at a frequency of 0.55 Hz with the dominant wave direction of −61° from the horizontal, consistent with the time series directional analysis. Interestingly, the directional spreading function at the peak frequency is much narrower than the wave age dependent functions given by Mitsuyasu et al. (1975) and Hasselmann et al. (1980). The results of Young and Van Vledder (1993) suggest that nonlinearities typically dominate the spreading shape while wind input is of lesser significance. Based upon the time series for all VWGs in Fig. 6, the value of wave steepness ak is 0.15–0.20, where a and k are the wave amplitude and wave number, respectively. Wave breaking was also occasionally observed (see Fig. 5), further supporting the climate of highly nonlinear waves during the measurements. The directional spreading function obtained by the array of VWGs compares well with the wave age independent directional spreading function of Donelan et al. (1985), consistent with the findings that nonlinearities, not wave age, play a major role in spreading shape (Young, 1994; Ewans, 1998).

Finally, the wave direction obtained from the VWG array is compared with the estimate obtained from the ATSIS point cloud method. Based upon the wave crest orientation and motion in consecutive water surface displacement maps, the wave propagation

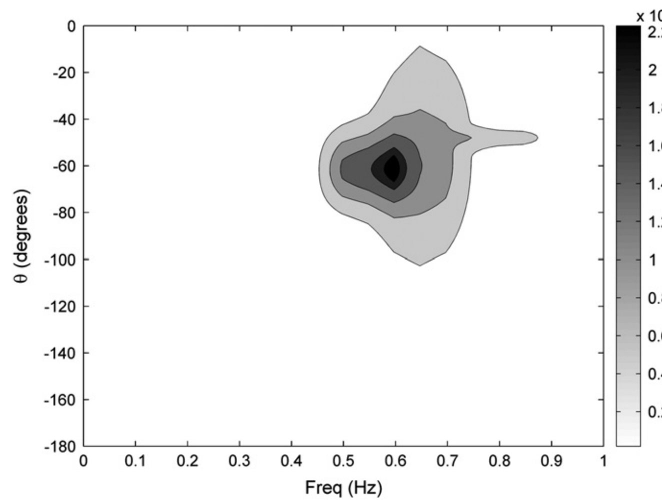

Fig. 7. Directional spectrum of the VWG array time series with peak at frequency 0.55 Hz and direction −61°.

angle was found to be –59° from the horizontal (see Fig. 10 in Wanek and Wu, 2006). The angle is very close to those estimated from both the time-series analysis (−60°) and directional wave spectrum (−61°) of the VWG array, further confirming the capability of the VWG to measure the direction of wave propagation. From the computational aspect, a total of 60,702 matching points are used to generate the ATSIS point clouds. In contrast, the wave direction obtained from the three time series of VWGs A, B, and C requires an average of 3.2 stereo matches per time step for a total of 2910 matching points over the course of 30 s time series, a 95% reduction from the point cloud method. The results indicate that the VWG array technique dramatically improves the computational efficiency in comparison with the ATSIS point cloud method. In addition, the VWG array technique provides an array of time series of water surface displacements as well as directional information. Finally, the flexibility of the VWG technique developed in this paper makes the offshore wave measurement feasible and simple in comparison with the traditional wave staff measurements.

4.2. Nearshore wave interaction with structures

The second experiment tests the capability of the VWG array technique to characterize nearshore waves interacting with a coastal structure. As seen in Fig. 8, the impermeable rock-mounted structure

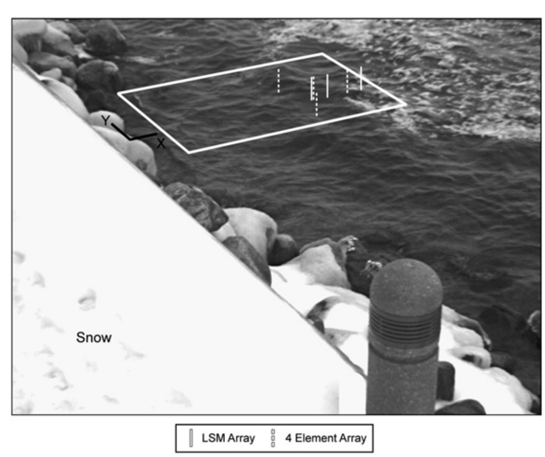

Fig. 8. VWG array locations for the reflection coefficient measurement, a four element star array of radius 0.5 m located 2.5 m away from the reflecting surface.

with a slope of unity acts as a reflective wall for the incoming waves generated by 3.1 m/s winds from the northwest direction. It is recognized that measuring a reflective wave climate near coastal structures in the field is not a simple task (Teisson and Benoit, 1994; Davidson et al., 1998; Zanuttigh and van der Meer, 2008). We conducted this experiment in the winter of 2009 while the air temperature was −8 °C and a small amount of ice was formed on the lake, making conventional wave measurements even more challenging. The ATSIS cameras were placed 3.9 m above the water surface with a 37 cm baseline and acquired images at 10 Hz for 120 s. A preliminary VWG time series analysis gives a dominant wave period of 1.5 s with a significant wave height of 0.13 m. The coastal structure is characterized by the reflection coefficient K, a ratio of reflected and incident wave height. An empirical reflection coefficient relationship gives $K_{empirical}=0.46$, obtained from the structure slope ($m\sim1$), significant wave height, and dominant wavelength (Zanuttigh and van der Meer, 2008). In the following, we estimate reflection coefficients using both the point cloud area method and various VWG arrays (see the white box region in Fig. 8).

Fig. 9 shows a consecutive time series of three-dimensional topographic water surface maps generated by the point cloud area method. The corresponding water surface contour maps are given in Fig. 10. The contour map (see Fig. 10a) identifies the incident wave propagating from the right and the reflected wave propagating from the left at $t=0$ s. The incident wavelength is estimated to be 2.2 m with a slightly oblique (~10°) orientation to the reflecting wall. At $t=0.1$ s (Fig. 10b), the two waves meet and superpose to yield a larger wave. Afterwards at $t=0.2$ s (Fig. 10c), the incident and reflected waves separate and pass each other. The propagation of the incident and reflective waves near the wall is clearly depicted. Based upon the wave crest elevations for the incident and reflected waves on the contour maps, the estimated reflection coefficient is $K_{point\ cloud}=H_R/H_I=0.45$, where H_I and H_R are the incident and reflected wave heights, respectively. The measured $K_{point\ cloud}$ is close to the empirical reflection coefficient $K_{empirical}$ of 0.46. Overall, the point cloud area method can provide a detailed temporal three-dimensional surface wave characteristics including propagation of waves and wave heights, facilitating an estimate of reflection coefficient near coastal structures.

Arrays of VWGs are also used to examine the reflection near the structure. We first setup a linear array (see Fig. 11a). The time series of surface displacements for the VWG linear array is processed using the least squares method (Goda and Suzuki, 1976) that assumes waves to be normally incident to reflective wall. Teisson and Benoit (1994) noted that for an incident angle less than 30°, the effect of oblique incidence on reflection coefficient measurement is negligible. In our case, since the slightly oblique incident wave angle is less than 10°, the use of a linear array is justified. Following the guidelines given by Mansard and Funke (1980), we determine the array placement and gauge spacing. Fig. 11b shows the power density spectrum of the incident and reflected wave components. Since wave energy is proportional to the square of wave height, the reflection coefficient can be estimated with a ratio of reflected wave energy to incident wave energy

$$K_{LSM}=\sqrt{\int_{f_{min}}^{f_{max}}S_R(f)df\Big/\int_{f_{min}}^{f_{max}}S_I(f)df}, \tag{6}$$

where $f_{\max}$ and $f_{\min}$ define the frequency range over which the reflection coefficient is computed and $S_R(f)$ and $S_I(f)$ are the reflected and incident wave spectrum, respectively. The calculated reflection coefficient for both the peak frequency and the dominant wave band of $0.5<f<0.8$ Hz is 0.48, a 4% difference from the empirical reflection coefficient $K_{empirical}$. Overall, this result demonstrates that the flexibility in gauge arrangement of the VWG technique allows for easy and adaptive placement to remotely measure reflection coefficients near a coastal structure.

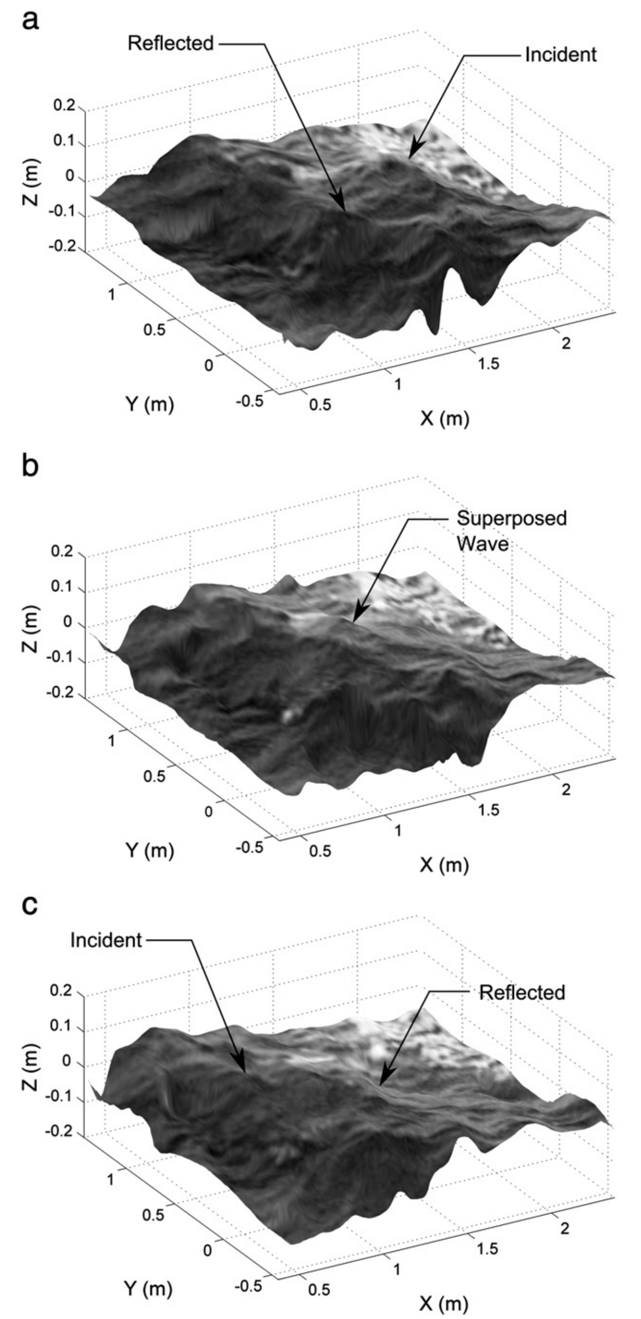

Fig. 9. Local reflection evolution from the area indicated in Fig. 8 at (a) $t=0.0$ s: reflected wave on the left and incident wave on the right, (b) $t=0.1$ s: superposition creates large wave, and (c) $t=0.2$ s: reflected wave (right) and incident wave (left) propagate past each other.

Directional arrays are further implemented to calculate the reflection coefficient using EMEP spectral analysis. Two factors, array design and array location, are critical to the accuracy of the estimate of reflection coefficient. First, Haubrich (1968) suggested that the key to array design is the coarray, which is the collection of vector spacing between the array components. Array performance is best when the coarray is uniformly distributed with a minimum gauge separation that avoids aliasing of wave components (Davis and Reiger, 1977; Young, 1994). In this study, we use 4-, 6-, and 15-element arrays that have the optimal coarrays (see Fig. 12), as presented by Haubrich (1968). Second, the array cannot be located near the reflector because EMEP cannot resolve reflection under the phase-

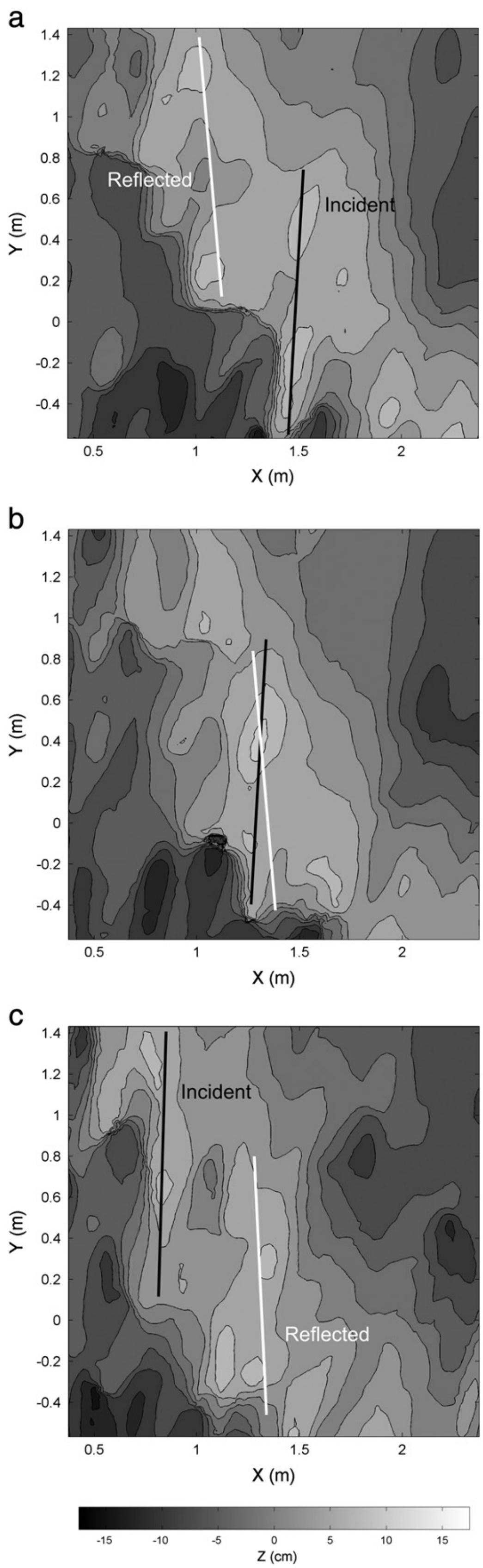

Fig. 10. Elevation contour plots corresponding to Fig. 9.

locked conditions that occur close to the reflector due to standing waves. To indicate where phase-locking affects directional array measurements, Huntley and Davidson (1998) introduced a non-

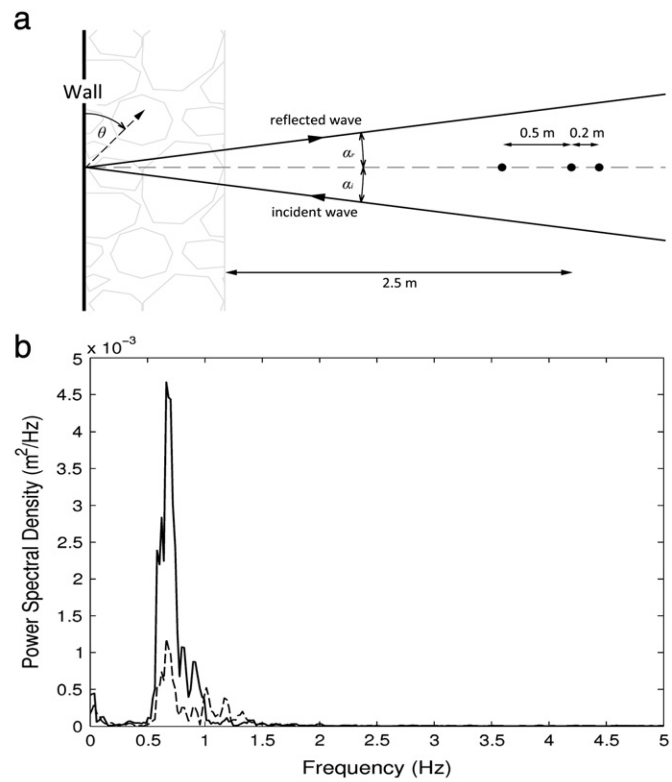

Fig. 11. Least squares method (a) linear VWG array setup and (b) resulting incident (solid line) and reflected (dashed line) frequency spectrum.

dimensional parameter L/S, where S is the length of the spectral analysis segment and L is the time lag between when the incident wave passes over the sensor and when the reflected wave returns. The time lag is defined as $L = 2d/c$, where d is the distance from the sensor to the reflector and c is the wave celerity. The analysis of Huang et al. (2003) indicates that EMEP is accurate for $L/S \geq 0.15$. To meet this guideline, we place the VWG arrays 2.5 m away from the wall, as seen in Fig. 12. The VWG arrays are processed over 120 s for a total analysis of 1200 images. Afterwards, the wave directional spectrum is calculated with a spectral window length of 256 data points. Based upon the directional spectrum the reflection coefficient is calculated as

$$K_{EMEP} = \sqrt{\int_{f_{min}}^{f_{max}} E_R(f)df \Big/ \int_{f_{min}}^{f_{max}} E_I(f)df}, \tag{7}$$

where $E_I(f) = \int_{180°}^{360°} S(f,\theta)d\theta$ E_I and $E_R(f) = \int_{0°}^{180°} S(f,\theta)d\theta$ are the incident and reflected wave energies, respectively.

Fig. 13 shows the directional spectrum of the wave field for (a) 4-element, (b) 6-element, and (c) 15-element VWG arrays. All directional spectra are bimodal with two distinct regions: an incident wave energy at θ~275° and a reflected wave energy at θ~95°. Reflection coefficients are summarized in Table 1. Overall, the calculated reflection coefficients are in good agreement with each other and within 10% of K_{LSM} and $K_{empirical}$ except for the 4-element array. The discrepancy can be due to a lower resolution of the 4-element array for processing bimodal spectrum in nearshore wave fields (Young et al., 1995). In other words, the technique in this paper improves the accuracy of nearshore wave field characterization by simply increasing the number of VWGs when required. Furthermore, we examine the effects of data duration by reducing from the analysis period from 120 s to 60 s. Note that conventional frequency spectrum analysis requires the wave field being stationary and random Gaussian process (Liu, 2000). In this study it is found that the reflection coefficients for the 4 or 6-element arrays based upon 60 s

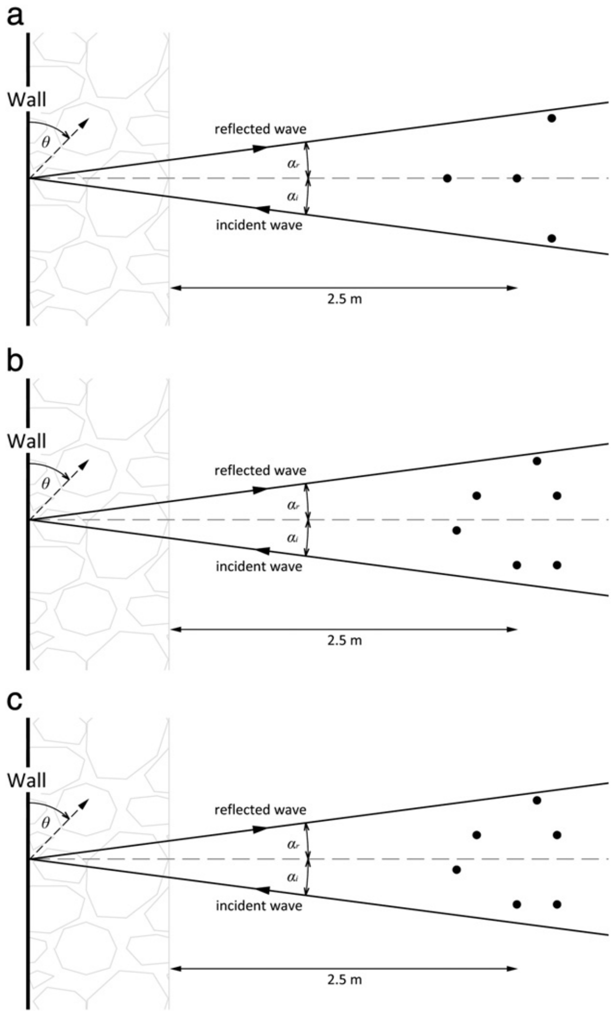

Fig. 12. Reflection array layouts for (a) 4 element array of 0.5 m spacing, (b) 6 element array of 0.25 m spacing, and (c) 15 element array of 0.125 m spacing.

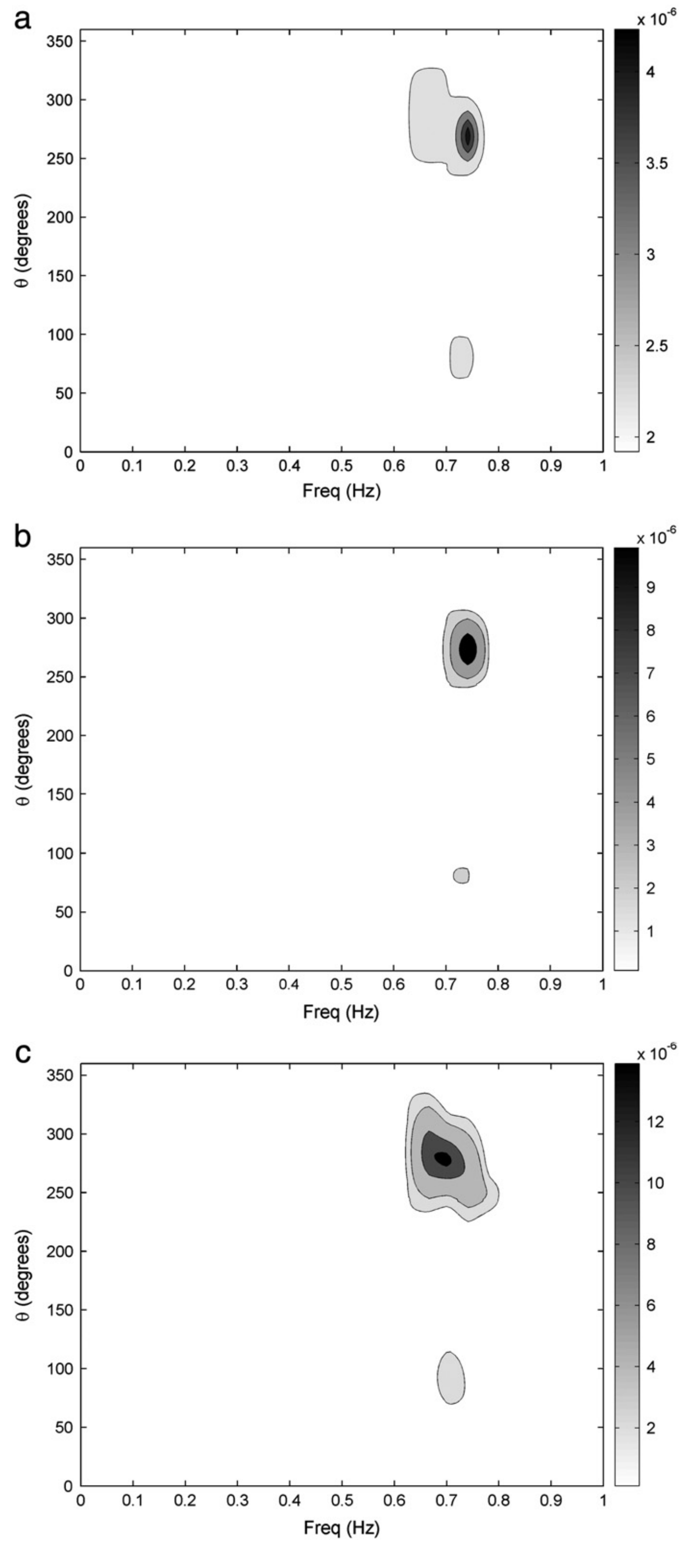

Fig. 13. Directional spectrum obtained from (a) 4 element array, (b) 6 element array, and (c) 15 element array.

differ to those based upon 120 s by up to 44%. Nevertheless for the 15-element array, the reflection coefficients based upon 60 and 120 s are within 10%, suggesting that increased spatial information from more VWGs can be used to characterize a non-stationary local wave field in lieu of a longer temporal record. Overall it is believed that the advantage of flexible number of VWGs in an array provides an effective resolution for the analysis of non-stationary properties like freak waves (Liu and Pinho, 2004; Wu and Yao, 2004).

Finally, in terms of computational cost, running each VWG takes an average of 3.8 stereo matches per time step. For the duration of the analysis period (i.e., 120 s), the total computational cost ranges from 13,680 matches for the 3-element linear array to 34,200 matches for the 15-element directional array. In comparison, the point cloud method requires 75,000 stereo matching points at a single instant in time to obtain a reflection coefficient, five times more computation than a VWG array. Furthermore, the point cloud method would need multiple time instants (at least three time steps) to reliably estimate the reflection coefficient based upon the wave height of incident and reflected waves (see Fig. 10). This comparison further supports the dramatic improvement in computational efficiency of VWG array technique over the ATSIS point cloud method.

5. Summary and conclusions

An innovative virtual wave gauge technique is developed to reduce the computational costs of stereo imaging for water wave measurement. In contrast to the Lagrangian–Eulerian point cloud method of previous stereo imaging studies on waves (Wanek and Wu, 2006), the VWG technique uses a Eulerian approach to track the elevation of the water surface at individual measurement points of interest (MPOI), dramatically reducing computational cost. By establishing a range of possible water surface elevations at an MPOI, the location of the water surface is constrained to a single line in an

Table 1
Reflection coefficients determined from virtual wave gauge arrays.

Method	120 s		60 s	
	Kr_{peak}	Kr_{band}	Kr_{peak}	Kr_{band}
Linear array	0.48	0.48	–	–
4 element array	0.61	0.44	0.34	0.28
6 element array	0.44	0.46	0.40	0.31
15 element array	0.51	0.46	0.50	0.42

image. An efficient dynamic searching algorithm based on weighted bisection is used to determine the location of the MPOI on the VWG. When validated against an *in situ* wire wave gauge, the VWG significant wave height is within 1.9% of the wire wave gauge measurement. Compared to the point cloud method, the VWG technique uses two orders of magnitude fewer stereo matched points. Overall the VWG is proven to be a highly accurate and computationally efficient wave measurement technique.

Wave direction is resolved by creating a spatial array of VWG in the image. The arrangement of the VWG array is adaptable based on wave conditions, allowing for direction to be resolved for a range of wavelengths. Owing to the ease of defining a VWG, complex array arrangements can be easily arranged based on changing wave climate to obtain the necessary array size and location. The flexibility of the VWG array is illustrated in two field applications. First, a right triangle array of VWGs is used to determine the directional spectrum of an offshore breaking wave field. The dominant wave direction determined by the VWG array is consistent with the crest orientations obtained from an instantaneous point cloud measurement. The total computation for the VWG array is found to have a 95% reduction from that by the point cloud method. For the second application, an array of VWG is placed in the nearshore to investigate waves interacting with a coastal structure. Both linear and directional VWG arrays are designed and located based on *a priori* information of the wave field. The reflection coefficient of the rock-mounted wall is computed from the VWG array data and is within 10% agreement with an empirical estimate of reflection coefficient based on wall type and geometry. Based on the demonstrated flexibility and computational efficiency, the VWG technique has the potential to make real-time remote stereo imaging wave measurements a reality.

Acknowledgements

This work was supported by the National Science Foundation, US Office of Naval Research, University of Wisconsin Sea Grant, and the Morgridge Fellowship. The authors would like to thank Professor Li Zhang for offering his expertise on computer vision and stereo imaging. In addition the assistance in data collection and advice on image processing from Mr. Justin Wanek and Alex Campbell are greatly appreciated.

References

Banner, M.L., Jones, I.S.F., Trinder, J.C., 1989. Wavenumber spectra of short gravity waves. Journal of Fluid Mechanics 198, 321–344.
Benetazzo, A., 2006. Measurements of short water waves using stereo matched image sequences. Coastal Engineering 53 (12), 1013–1032.
Benoit, M., Teisson, C., 1994. Laboratory comparison of directional wave measurement systems and analysis techniques. Proceedings of the 24th International Conference on Coastal Engineering. ASCE, Kobe, Japan, pp. 42–56.
Bhat, D.N., Nayar, S.K., 1998. Stereo and specular reflection. International Journal of Computer Vision 26 (2), 91–106.
Bock, E.J., Hara, T., 1995. Optical measurements of capillary-gravity wave spectra using a scanning laser slope gauge. Journal of Atmospheric and Oceanic Technology 12 (2), 395–403.
Bréon, F.M., Henriot, N., 2006. Spaceborne observations of ocean glint reflectance and modeling of wave slope distributions. Journal of Geophysical Research 111 (C6), C06005. doi:10.1029/2005JC003343.
Brown, M.Z., Burschka, D., Hager, G.D., 2003. Advances in computational stereo. IEEE Transactions on Pattern Analysis and Machine Intelligence 25 (8), 993–1008.
Cox, C., Munk, W., 1954. Statistics of the sea surface derived from sun's glitter. Journal of Marine Research 13, 198–227.
Cureton, G.P., Anderson, S.J., Lynch, M.J., McGann, B.T., 2007. Retrieval of wind wave elevation spectra from sunglint data. IEEE Transactions on Geoscience and Remote Sensing 45 (9), 2829–2836.
Dankert, H., Rosenthal, W., 2004. Ocean surface determination from X-band radar-image sequences. Journal of Geophysical Research 109, C04016. doi:10.1029/2003JC002130.
Davidson, M.A., Huntley, D.A., Bird, P.A.D., 1998. A practical method for the estimation of directional wave spectra in reflective wave fields. Coastal Engineering 33 (2–3), 91–116.
Davis, R.E., Regier, L.A., 1977. Methods for estimating directional wave spectra from multi-element arrays. Journal of Marine Research 35, 453–477.
de Vries, S., Hill, D., de Schipper, M.A., Stive, M.J.F., 2009. Using stereo photogrammetry to measure coastal waves. Proceedings of the 10th International Coastal Symposium, Lisbon, Portugal: Journal of Coastal Research, SI, 56, pp. 1484–1488.
Dhond, U.R., Aggarwal, J.K., 1990. Binocular versus trinocular stereo. Proceedings of the IEEE International Conference on Robotics and Automation 3, 2045–2050 (Cincinnati, Ohio).
Donelan, M.A., Hamilton, J., Hui, W.H., 1985. Directional spectra of wind-generated waves. Philosophical Transactions of The Royal Society A Mathematical Physical and Engineering Sciences 315 (1534), 509–562.
Ewans, K.C., 1998. Observations of the directional spectrum of fetch-limited waves. Journal of Physical Oceanography 28 (3), 495–512.
Forsyth, D.A., Ponce, J., 2003. Computer vision: a modern approach. Upper Saddle River. Pearson Education, New Jersey. 693 pp.
Frew, N.M., Bock, E.J., Schimpf, U., Hara, T., Haussecker, H., Edson, J.B., McGillis, W.R., Nelson, R.K., McKenna, S.P., Us, B.M., Jähne, B., 2004. Air–sea gas transfer: its dependence on wind stress, small-scale roughness, and surface films. Journal of Geophysical Research 109, C08S17. doi:10.1029/2003JC002131.
Goda, Y., Suzuki, Y., 1976. Estimation of incident and reflected waves in random wave experiments. Proceedings of the 15th Coastal Engineering Conference, vol. 1. ASCE, Honolulu, Hawaii, pp. 828–845.
Gotwols, B.L., Irani, G.B., 1980. Optical determination of the phase velocity of short gravity waves. Journal of Geophysical Research 85 (C7), 3964–3970.
Hara, T., Bock, E.J., Lyzenga, D., 1994. In situ measurements of capillary-gravity wave spectra using a scanning laser slope gauge and microwave radars. Journal of Geophysical Research 99 (C6), 12593–12602.
Hashimoto, N., 1997. Analysis of the directional wave spectra from field data. In: Liu, P.L.-F. (Ed.), Advances in Coastal and Ocean Engineering, Vol.3. World Scientific, Singapore, pp. 103–143.
Hasselmann, D.E., Dunckel, M., Ewing, J.A., 1980. Directional wave spectra observed during JONSWAP 1973. Journals of Physical Oceanography 10 (8), 1264–1280.
Haubrich, R.A., 1968. Array design. Bulletin. Seismological Society of America 58 (3), 977–991.
Herbers, T.H.C., Lentz, S.J., 2010. Observing directional properties of ocean swell with an acoustic Doppler current profiler (ADCP). Journal of Atmospheric and Oceanic Technology 27, 210–225.
Holland, K.T., Holman, R.A., Lippmann, T.C., Stanley, J., Plant, N., 1997. Practical use of video imagery in nearshore oceanographic field studies. IEEE Journal of Oceanic Engineering 22 (1), 81–92.
Holman, R.A., Stanley, J., 2007. The history and technical capabilities of Argus. Coastal Engineering 54 (6–7), 477–491.
Holthuijsen, L.H., 1983. Observations of the directional distribution of ocean-wave energy in fetch-limited conditions. Journal of Physical Oceanography 13 (2), 191–207.
Holthuijsen, L.H., 2007. Waves in Coastal and Oceanic Waters. Cambridge University Press, New York, NY. 404 pp.
Huang, W.P., Chou, C.R., Yim, J.Z., 2003. Experiments on the reflection coefficients of a detached breakwater in a directitonal wave field. Coastal Engineering 47 (4), 367–379.
Huntley, D.A., Davidson, M.A., 1998. Estimating the directional spectrum of waves near a reflector. Journal of Waterway, Port, Coastal and Ocean Engineering 124 (6), 312–319.
Hwang, P.A., Atakturk, S., Sletten, M.A., Trinza, D.B., 1996. A study of the wavenumber spectra of short water waves in the ocean. Journal of Physical Oceanography 26 (7), 1266–1285.
Hwang, P.A., Wang, D.W., Walsh, E.J., Krabill, W.B., Swift, R.N., 2000. Airborne measurements of the wavenumber spectra of ocean surface waves. Part I: spectral slope and dimensionless spectral coefficient. Journal of Physical Oceanography 30 (11), 2753–2767.
Hwung, H.H., Kuo, C.A., Chien, C.H., 2009. Water surface level profile estimation by image analysis with varying overhead camera posture angle. Measurement Science and Technology 20 (7) Art. #: 075104.
Irish, J.L., Wozencraft, J.M., Cunningham, A.G., Giroud, C., 2006. Nonintrusive measurement of ocean waves: lidar wave gauge. Journal of Atmospheric and Ocean Technology 23 (11), 1559–1572.
Jähne, B., Klinke, J., Waas, S., 1994. Imaging of short ocean wind waves: a critical theoretical review. Journal of the Optical Society of America 11 (8), 2197–2209.
Jähne, B., Reimer, K.S., 1990. Two-dimensional wave number spectra of small-scale water surface waves. Journal of Geophysical Research 95 (C7), 11531–11546.
Jähne, B., Schmidt, M., Rocholz, R., 2005. Combined optical slope/height measurements of short wind waves: principle and calibration. Measurement Science and Technology 16 (10), 1937–1944.
Johnson, D., 2008. DIWASP, a directional wave spectra toolbox for MATLAB®: user manual. Research Report WP-1601-DJ (V1.1), Centre for Water Research, University of Western Australia.

Keller, W.C., Gotwols, B.L., 1983. Two-dimensional optical measurement of wave slope. Applied Optics 22 (22), 3476–3478.
Kim, B.O., Cho, H.Y., Lim, D.I., Yoon, G.L., Oh, I.S., Park, Y.A., 2008. Nearshore wave measurement using single-video images of buoy motions. Journal of Coastal Research 24 (6), 1481–1486.
Krogstad, H.E., Barstow, S.F., Aasen, S.E., Rodriguez, I., 1999. Some reent developments in wave buoy measurement technology. Coastal Engineering 37 (3–4), 309–329.
Liu, P.C., 2000. Is the wind wave frequency spectrum outdated. Ocean Engineering 27 (5), 577–588.
Liu, P.C., Pinho, U.F., 2004. Freak waves—more frequent than rare! Annaels Geophysicae 22 (5), 1839–1842.
Mansard, E.P.D., Funke, E.R., 1980. The measurement of incident and reflected spectra using a least squares method. Proceedings of the 17th International Conference on Coastal Engineering, vol. 1. ASCE, Sydney, Australia, pp. 151–172.
Mitsuyasu, H., Tasai, F., Suhara, T., Mizuno, S., Ohkusu, M., Honda, T., Rikiishi, K., 1975. Observations of the directional spectrum of ocean waves using a cloverleaf buoy. Journal of Physical Oceanography 5 (4), 750–760.
Palm, C.S., Anderson, R.C., Reece, A.M., 1977. Laser prove for measuring 2-D wave slope spectra of ocean capillary waves. Applied Optics 16 (4), 1074–1081.
Savelsberg, R., Holten, A., de Water, W.V., 2006. Measurement of the gradient field of a turbulent free surface. Experiments in Fluids 41 (4), 629–640.
Scharstein, D., Szeliski, R., 2002. A taxonomy and evaluation of dense two-frame stereo correspondence algorithms. International Journal of Computer Vision 47 (1–3), 7–42.
Shemdin, O.H., Hwang, P.A., 1988. Comparison of measured and predicted sea surface spectra of short waves. Journal of Geophysical Research 99 (C11), 13883–13890.
Shemdin, O.H., Tran, H.M., Wu, S.C., 1988. Directional measurement of short ocean waves with stereophotography. Journal of Geophysical Research 93 (C11), 13891–13901.
Steele, K.E., Teng, C.C., Wang, D.W.C., 1992. Wave direction measurements using pitch-roll buoys. Ocean Engineering 19 (4), 349–375.
Stilwell, D., 1969. Directional energy spectra of the sea from photographs. Journal of Geophysical Research 74 (8), 1974–1986.
Su, W., Charlock, T.P., Rutledge, K., 2002. Observations of reflectance distribution around sunglint from a coastal ocean platform. Applied Optics 41 (35), 7369–7383.
Sun, J., Burns, S.P., Vandemark, D., Donelan, M.A., Mahrt, L., Crawford, T.L., Herbers, T.H.C., Crescenti, G.H., French, J.L., 2005. Measurement of directional wave spectra using aircraft laser altimeters. Journal of Atmospheric and Oceanic Technology 22 (7), 869–885.
Teisson, C., Benoit, M., 1994. Laboratory measurement of oblique irrectular wave reflection on rubble-mound breakwaters. Proceedings of the 24th International Conference on Coastal Engineering. ASCE, Kobe, Japan, pp. 1610–1624.
Terray, E.A., Brumley, B.H., Strong, B., 1999. Measuring waves and currents with an upward-looking ADCP. Proceedings of the IEEE 6th Working Conference on Current Measurement (San Diego, California), pp. 66–71.
Tucker, M.J., Pitt, E.G., 2001. Waves in Ocean Engineering. Elsevier Ocean Engineering Book Series. Vol. 5. Oxford, Elsevier Science, United Kingdom, 67-76 and 255-258.
Van Haren, H., 2001. Estimates of sea level, waves and winds from a bottom-mounted ADCP in a shelf sea. Journal of Sea Research 45 (1), 1–14.
Wanek, J.M., Wu, C.H., 2006. Automated trinocular stereo imaging system for three-dimensional surface wave measurements. Ocean Engineering 33 (5–6), 723–747.
Wu, C.H., Yao, A., 2004. Laboratory measurements of limiting freak waves on currents. Journal of Geophyiscal Research-Oceans 109 (C12), 1–18, C12002. doi:10.1029/2004JC002612.
Wolf, P., DeWitt, B., 2000. Elements of Photogrammetry: with Applications in GIS. McGraw-Hill, Boston, Massachusetts. 608 pp.
Wyatt, L.R., Thompson, S.P., Burton, R.R., 1999. Evaluation of high frequency radar wave measurement. Coastal Engineering 37 (3–4), 259–282.
Yao, A., Wu, C.H., 2005. An automated image-based technique for tracking sequential surface wave profiles. Ocean Engineering 32 (2), 157–173.
Young, I.R., 1994. On the measurement of directional wave spectra. Applied Ocean Research 16 (5), 283–294.
Young, I.R., Van Vledder, G.P., 1993. A review of the central role of nonlinear interactions in wind wave evolution. Philosophical Transactions of the Royal Society of London 342 (1666), 505–524.
Young, I.R., Verhagen, L.A., Banner, M.L., 1995. A note on the bimodal directional spreading of fetch-limited wind waves. Journal of Geophysical Research 100 (C1), 733–778.
Zanuttigh, B., van der Meer, J.W., 2008. Wave reflection from coastal structures in design conditions. Coastal Engineering 55 (10), 771–779.
Zappa, C.J., Banner, M.L., Schultz, H., Corrada-Emmanuel, A., Wolff, L.B., Yalcin, J., 2008. Retrieval of short ocean wave slope using polarimetric imaging. Measurement Science and Technology 19 (5), 055503.
Zhang, X., Cox, C., 1994. Measuring the two-dimensional structure of a wavy water surface optically: a surface gradient detector. Experiments in Fluids 17 (4), 225–237.